PHYSICAL REVIEW MATERIALS **1**, 060601(R) (2017)

Structural imaging of nanoscale phonon transport in ferroelectrics excited by metamaterial-enhanced terahertz fields

Yi Zhu,[1] Frank Chen,[2,3] Joonkyu Park,[4] Kiran Sasikumar,[5] Bin Hu,[1] Anoop R. Damodaran,[6,7] Il Woong Jung,[5] Matthew J. Highland,[8] Zhonghou Cai,[1] I-Cheng Tung,[1] Donald A. Walko,[1] John W. Freeland,[1] Lane W. Martin,[6,7] Subramanian K. R. S. Sankaranarayanan,[5] Paul G. Evans,[4] Aaron M. Lindenberg,[3,9,10] and Haidan Wen[1,*]

[1]*Advanced Photon Source, Argonne National Laboratory, Argonne, Illinois 60439, USA*
[2]*Department of Electrical Engineering, Stanford University, Stanford, California 94305, USA*
[3]*SIMES Institute for Materials and Energy Sciences, SLAC National Accelerator Laboratory, Menlo Park, California 94025, USA*
[4]*Department of Materials Science and Engineering, University of Wisconsin, Madison, Madison, Wisconsin 53706, USA*
[5]*Center for Nanoscale Materials, Argonne National Laboratory, Argonne, Illinois 60439, USA*
[6]*Department of Materials Science and Engineering, University of California, Berkeley, Berkeley, California 94720, USA*
[7]*Materials Sciences Division, Lawrence Berkeley National Laboratory, Berkeley, California 94720, USA*
[8]*Materials Science Division, Argonne National Laboratory, Argonne, Illinois 60439, USA*
[9]*Department of Materials Science and Engineering, Stanford University, Stanford, California 94305, USA*
[10]*PULSE Institute, SLAC National Accelerator Laboratory, Menlo Park, California 94025, USA*

(Received 13 September 2017; published 16 November 2017)

Nanoscale phonon transport is a key process that governs thermal conduction in a wide range of materials and devices. Creating controlled phonon populations by resonant excitation at terahertz (THz) frequencies can drastically change the characteristics of nanoscale thermal transport and allow a direct real-space characterization of phonon mean-free paths. Using metamaterial-enhanced terahertz excitation, we tailored a phononic excitation by selectively populating low-frequency phonons within a nanoscale volume in a ferroelectric $BaTiO_3$ thin film. Real-space time-resolved x-ray diffraction microscopy following THz excitation reveals ballistic phonon transport over a distance of hundreds of nm, two orders of magnitude longer than the averaged phonon mean-free path in $BaTiO_3$. On longer length scales, diffusive phonon transport dominates the recovery of the transient strain response, largely due to heat conduction into the substrate. The measured real-space phonon transport can be directly compared with the phonon mean-free path as predicted by molecular dynamics modeling. This time-resolved real-space visualization of THz-matter interactions opens up opportunities to engineer and image nanoscale transient structural states with new functionalities.

DOI: 10.1103/PhysRevMaterials.1.060601

The continuous decrease in size and increase in unit density, operating speeds, and dissipation in nanoscale materials has led to the creation of devices in which the fundamental length scale of heat transport is no longer well-described by conventional thermal diffusion [1]. When the functional unit of a device, e.g., the channel of a transistor, is smaller than the mean-free path (MFP) of energy carriers, energy transport enters a new regime dominated by ballistic rather than diffusive processes [2]. Phonons, the major heat carriers, and their nanoscale transport in materials, underpin the fundamental energy transport processes and the operation of modern electronic and optoelectronic devices. Characterization of the MFP of phonons is crucial to a fundamental description of microscopic energy flow in materials and to practical applications [2,3]. To access this ballistic regime on ultrafast time scales, optical excitation of engineered nanoscale structures was utilized to generate rapid local heating and the subsequent phonon transport was probed by optical [4–6] and x-ray [7] diffraction in reciprocal space. Although MFPs can be inferred from these measurements, a real-space tracking of energy transport such as lattice strain evolution is needed to directly characterize the spatially dependent structural dynamics that can be quantitatively compared with the first-principle calculations.

In contrast to optical excitation that typically leads to a broad frequency distribution of excited phonons, THz pulses with milli-electron-volt (meV) photon energy can selectively excite low-energy collective modes such as phonons, magnons, and eletromagnons [8–11], as well as manipulate electrical dipoles using the associated ultrafast electric fields. At THz frequencies, metamaterials can be used to manipulate THz radiation on a length scale orders of magnitude smaller than the THz wavelength [12–14], providing a unique nanoscale control of collective modes in materials, e.g., phonon transport in alloy-based nanomaterials [15]. The extreme confinement and drastic enhancement of THz fields at nanometer (nm) dimensions enable transient spatial engineering and biasing of material properties on ultrafast time scales. For example, metamaterial-enhanced THz fields have been used to induce an insulator-to-metal phase transition in VO_2 thin films [16,17], to manipulate ferroelectric polarization [18,19], to drive nonlinear phenomena in GaAs [20], and to achieve ultrastrong coupling of the cyclotron transition [21]. However, the spatial confinement of the enhanced field also makes it difficult to characterize these local and transient THz field-induced changes of material properties. As a result, probing material response following near-field-enhanced THz excitation usually relies on a macroscopic change of material properties [16], rather than a direct and local characterization

*wen@aps.anl.gov

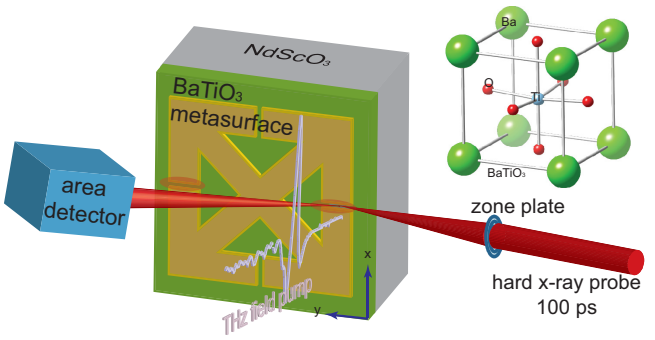

FIG. 1. Schematic of the experiment. The vertically polarized THz pulses are focused onto the sample surface. The THz field is enhanced near the horizontal gold gaps (red-colored ellipses) of the split-ring resonators shown by the gold color. An x-ray beam is focused by a Fresnel zone plate to probe locally in the vicinity of the field-enhanced regions and the diffracted x-ray beam is collected by an area detector. The inset shows the unit cell of $BaTiO_3$.

of the interactions. A time-resolved imaging technique capable of revealing localized light-matter interactions is critical for understanding nanoscale transient phenomena in materials.

In this work, we demonstrate the control and imaging of nanoscale phonon transport in a prototypical ferroelectric. In particular, metamaterial-enhanced intense THz fields are used to create phononic excitations that selectively populate low-frequency phonons with long MFPs within nanoscale volumes. The resultant time-dependent strain distribution within a $BaTiO_3$ (BTO) epitaxial thin film is directly measured by time-resolved hard x-ray diffraction (XRD) microscopy [22]. Time-resolved x-ray imaging provides not only real-time characterization sensitive to local structural properties but also finer spatial resolution than what can be achieved with optical microscopy due to diffraction limit set by the optical wavelength [23,24]. The evaluation of ballistic phonon transport in real space demonstrates a unique capability for studying nanoscale thermal transport beyond spatially averaged ultrafast probes [4,5,7,25] and temporally averaged high spatial resolution probes [26]. We find that THz excitation produces a highly localized strain profile that broadens by a few hundred nm over a time interval of 100 ps. The broadening cannot be explained by diffusive thermal transport, but agrees well with ballistic phonon transport with a MFP of ∼500 nm, which is significantly longer than the frequency-averaged phonon MFP of 2 nm in BTO at room temperature [27]. The increase in the MFP is due to selective excitation of low-energy phonons with long MFPs by the THz field, in agreement with molecular dynamics calculations. On longer time scales, the recovery of the strain profile occurs by heat diffusion into the substrate. These measurements of the time-dependent strain profile constitute a direct visualization of the near-field THz interaction in a ferroelectric material and reveal in-plane ballistic phonon transport, resolving a long-standing characterization and imaging challenge.

The THz-pump/x-ray probe microscopy studies (Fig. 1) were conducted at 7-ID-C beamline of the Advanced Photon Source (APS). A 90 nm-thick BTO thin film was grown epitaxially on a $NdScO_3$ (NSO) orthorhombic (110) single-crystal substrate by pulsed laser deposition. Split-ring resonators (SRRs) were fabricated on the thin-film surface using a photolithography lift-off method to pattern a 100-nm-thick gold film. The SRR occupies an area of $50 \times 50\,\mu m^2$ with a 2.7-μm gap on each of the four edges. Intense THz pulses with a central frequency of 0.6 THz were generated using the pulse-front-tilt technique [28] at a 1-kHz repetition rate. The vertically polarized THz pulses were focused by a pair of off-axis parabolic mirrors onto the sample surface with a measured field intensity of 200 kV/cm at the focus using electro-optical sampling [29]. Horizontally polarized hard x-ray pulses from the APS storage ring with 11-keV photon energy and 100-ps pulse duration were focused onto the sample surface by a Fresnel zone-plate. The sample was mounted vertically as shown in Fig. 1. In this configuration, the vertical spatial resolution along the x axis was determined by the x-ray full width at half maximum of 420 nm, although the horizontal spatial resolution along the y axis was approximately 2.5 μm due to larger x-ray horizontal beam size and the x-ray footprint at ∼16° incident angle.

We first characterized the strain distribution of the BTO film in the absence of THz excitation. Figure 2(a) shows the diffracted 11-keV x-ray intensity recorded at the fixed incident angle of 16.09° on the lower angle side of the BTO 002 Bragg peak, while the sample was raster scanned along x and y directions. The lower diffraction intensity of the BTO film underneath the gold film is due to a shift of the Bragg peak to a higher angle. To assess this shift quantitatively, the BTO 002 Bragg peaks in the SRR gap region and underneath the gold film were measured. Figure 2(b) shows that there is a 0.3% out-of-plane lattice contraction of the BTO film under the gold metamaterial. This strain variation due to the gold film needs to be subtracted in the time-resolved measurements as shown later.

The structural response of the BTO film following THz excitation was evaluated by comparing the 002 Bragg reflection measured at a fixed location of $x = 1.5\,\mu$m and $y = 0$ within the SRR gap before and after the THz excitation. The THz excitation induces a shift of the Bragg reflection to a lower angle measured at a delay time of 100 ps after excitation [Fig. 2(c)], corresponding to a 0.04% lattice expansion along the out-of-plane direction. This is associated with a direct excitation of the ionic vibrational degrees of freedom in BTO by the intense THz field [18]. In Fig. 2(d), the THz-induced diffraction intensity change at the x-ray incident angle of 16.09° is plotted as a function of delay. Since the diffraction intensity measured at the low-angle side of the Bragg peak is proportional to the angular shift of the diffraction peak for small strain, the intensity change can be converted to an out-of-plane strain, as shown by the right vertical axis in Fig. 2(d). The peak intensity increases as the diffraction peak shifts to lower angles, and recovers on tens of ns timescales, in agreement with the thermal transport time scale from the thin film to the substrate [18].

To gain insight into the localized interaction of the THz field and the ferroelectric, the diffraction intensity was recorded at a fixed delay time (100 ps) and diffraction angle (16.09°) while scanning the sample position. We subtracted the intensity map measured before the THz excitation from that measured at 100 ps to eliminate the static strain variation of the BTO

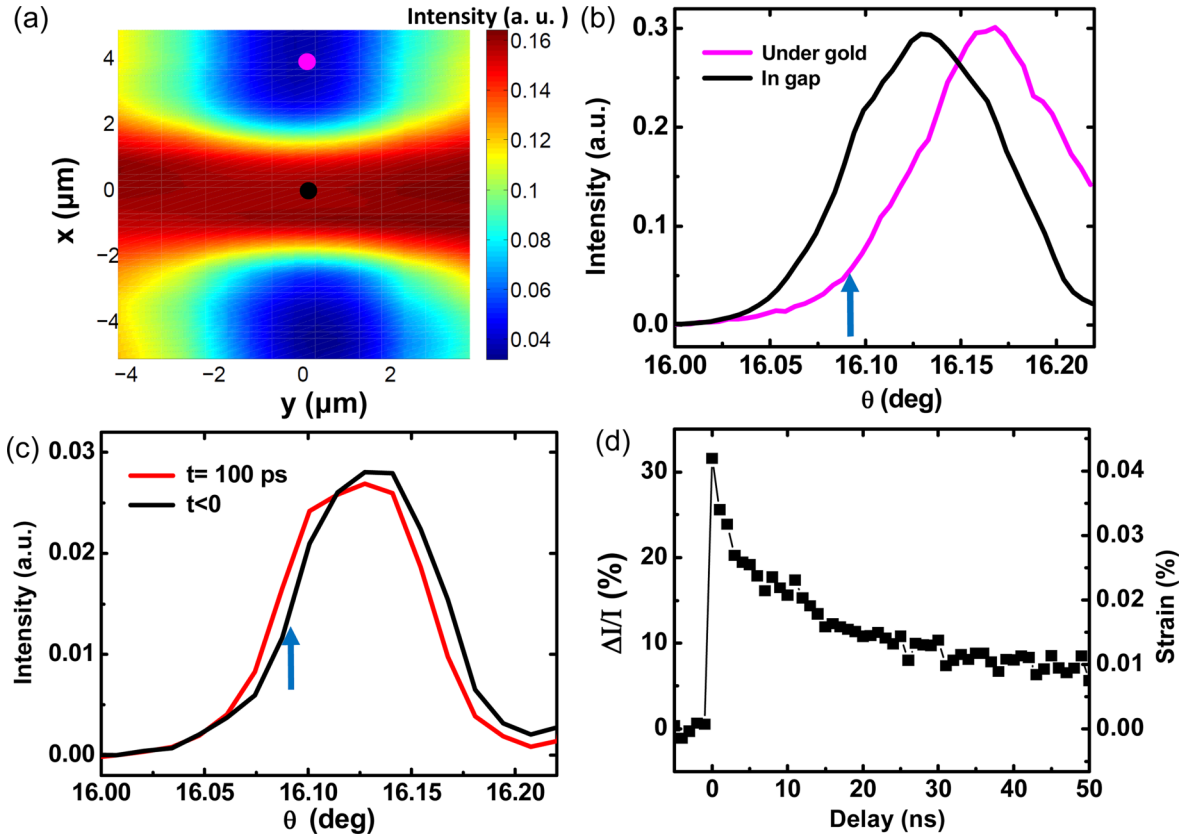

FIG. 2. (a) Static x-ray diffraction intensity map of the sample around the SRR gap without THz excitation. (b) The radial scans of BTO 002 x-ray reflection in the gap and under the gold surface, corresponding to the positions shown by the color dots in (a). (c) The THz-induced shift of the 002 diffraction peak of the BTO thin film. The blue arrow indicates the diffraction angle $\theta = 16.09^{\circ}$ at which (a) and (d) plots were acquired. (d) The diffraction intensity change and the calibrated strain as a function of delay between THz and x-ray pulses.

film across the gap. The difference map thus only shows the THz-induced change of the diffraction intensity. The calibrated out-of-plane strain is shown in Fig. 3(a), which corresponds to an estimated maximal temperature increase of 70 K using the measured thermal expansion coefficient [18]. The location of the gold SRR structure near the split gap could be obtained simultaneously by monitoring the diffraction intensity from the gold film, shown in magenta in Fig. 3(a). The simultaneous measurement of gold diffraction intensity provides an independent and *in situ* characterization of the gold edge position, which is crucial to evaluate the sample position drift during data acquisition [30]. To study the evolution of the strain profile, we measured the one-dimensional strain profile along the dashed line in Fig. 3(a) at various delays, clearly resolving the double-peak strain profile and its recovery as shown in Fig. 3(b). Beyond 100 ps, the magnitude of the strain decreases while the strain profile does not show any significant broadening. After the experiments, neither visual damage nor structural degradation of the sample across the gap was observed using optical microscope and micro-XRD measurements, respectively.

In order to understand the measured time-dependent strain profiles, we first calculate the THz field distribution at time zero, as defined by the arrival time of the peak THz field at the sample. The THz field distribution around the gold gap was simulated using a frequency-domain solver in the CST-Microwave Studio. The frequency of the THz wave in the simulation is 0.6 THz, which is the central frequency of the pump THz pulse [Fig. 4(a)]. The simulation includes the SRR, BTO film, and NSO substrate stacked in the order shown on the bottom of Fig. 3(b). The THz peak field close to the edge of the gap is enhanced to 3 MV/cm in air. Considering the dielectric constant of BTO/NSO sample, the maximum THz peak field in the BTO layer is reduced to 1 MV/cm, corresponding to a factor of 5 field enhancement. The THz field distribution map in the BTO layer $|E(x,y,z_0)|$ is plotted in Fig. 4(b), where $z_0 = -50\,\text{nm}$, i.e., 50 nm below the gold surface shown as the dashed red line in Fig. 3(b), in the middle of the BTO layer. To ensure the accuracy of the THz field distribution, we modeled the exact shape of the SRR unit as used in the experiment, based on the scanning electron microscopy image of the sample. To show the line profile of the electric-field distribution in the x-ray probed region, the field distribution is averaged along the y axis of the white rectangular box across the gap shown in Fig. 4(b) [30]. The averaged field distribution $|E(x)|$ is plotted in Fig. 4(c). In order to investigate the dependence of the THz field distribution on the incident THz frequency, the THz electric-field distribution is calculated at various frequencies across the incident THz spectrum. After normalizing the calculated results at different THz frequencies, we found the width of the peaks does not change significantly except for small variations of the plateau

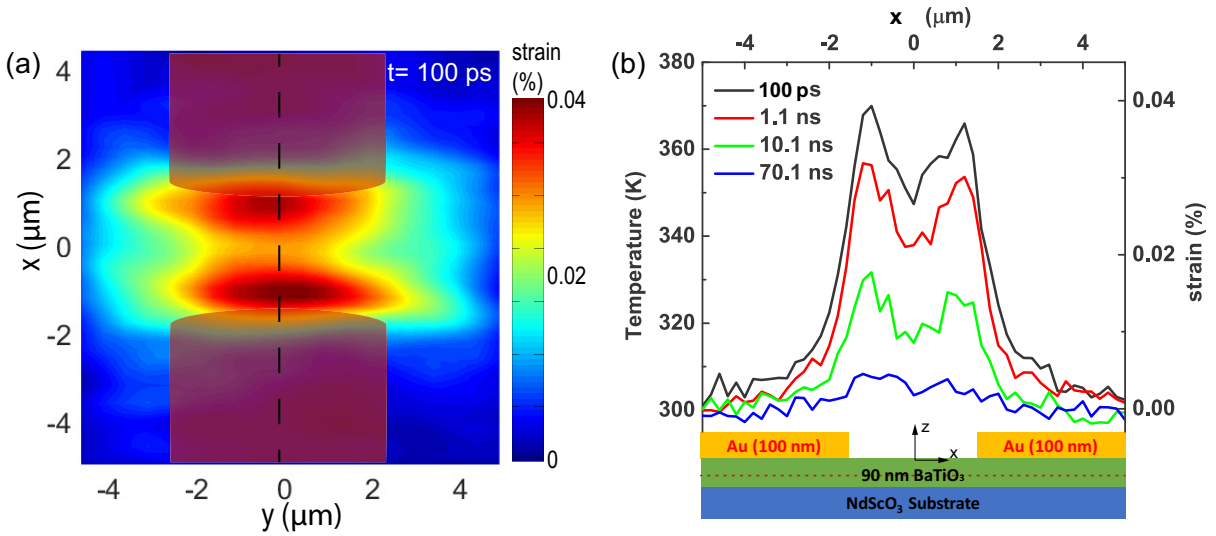

FIG. 3. (a) The THz-induced strain map obtained by subtracting the diffraction intensity map measured before THz excitation from the one measured at 100 ps after THz excitation. Two-dimensional smooth was applied. The magenta-overlaid area shows the gold metamaterial profile extracted from the intensity maps of the gold diffraction. (b) Strain profiles along the dashed line in (a) measured at different delays. The inset at the bottom of the plot shows a cross-sectional view of the sample. The THz field distribution is calculated along the dashed red line.

region in the middle of the gap [Fig. 4(c)]. Similar calculations by varying thicknesses and dielectric constants of BTO and NSO layers show the simulated double-peak width does not change within the uncertainties of the parameters used.

Based on the THz field distribution, we calculate the THz-induced strain, which is proportional to the absorbed THz energy [18] and thus is proportional to $|E|^2$. This strain profile upon THz excitation is used as the initial condition for simulating the strain profile at $t = 100$ ps by a diffusive thermal transport model [30]. The simulation results are then convolved with the x-ray beam profile to produce the expected strain profile as a result of diffusive thermal transport, which can be compared with the experimentally measured strain profile by x-ray diffraction microscopy [Fig. 4(d)]. To characterize the double-peak width, the simulated profiles are fit by two Gaussian peaks and a plateau in the gap [30]. The average half width at half maximum (HWHM) of double peaks at 0.6 THz is 350 ± 10 nm (the error bar shows the fitting error). A similar fit shows the peaks of the measured strain profile have an average HWHM of 815 ± 57 nm, much larger than 350 ± 10 nm predicted by the combination of diffusive thermal transport with the electric-field calculation. Therefore, the measured double-peak strain profile is significantly broader than the expected strain profile as a result of diffusive thermal transport.

To understand the observed broadening of the in-plane strain profile, we first exclude possible measurement errors such as instrumental broadening due to larger x-ray spot size and the position jitter of the x-ray beam with respect to the sample. A careful consideration of these errors [30] supports that the mismatch between the simulated and observed strain profiles at 100 ps is due to the intrinsic response of the BTO film to nanoscale THz excitation. The fact that the measured strain profile is broader than the prediction of the thermal diffusion model indicates that the thermal diffusion processes alone cannot explain the observed broadening at 100 ps, and a faster in-plane strain transport process must play a role.

The broadening of the strain profile can be described based on a ballistic phonon transport process [2,4] resulting from selective phonon excitation [31]. By approximating the strain front at the half rising point of the strain profile, the strain propagation speed can be calculated as the broadening of the HWHM from 350 to 815 nm, a 465-nm increase within 100 ps, which corresponds to a speed of 4.65 km/s. This gives a lower bound of the speed of propagation of the THz-excited phonon wave packet. The magnitude of this speed is much faster than the diffusive process and agrees with a ballistic thermal transport process in which the phonon wave packet travels at the speed of sound.

After 100 ps, the observed evolution of the strain profile is predominantly a thermal diffusive process. We employ thermal modeling of the diffusion process (COMSOL MULTIPHYSICS, COMSOL Inc.) with the sample geometry shown on the bottom of Fig. 3(b) to simulate the time-dependent temperature profile at various time delays [30]. We use the measured temperature profile at 100 ps as the initial condition shown as the black curve in Fig. 4(e). The simulated time-dependent temperature profiles at different times are shown as other color curves in Fig. 4(e). The shape and amplitude of the simulated profiles are in good agreement with the experimental results shown in Fig. 3(b). Kinks in the simulated BTO temperature profile close to the gold edge shown at 10.1 ns are not observed at 1.1 ns because the thermal transport from BTO to gold is not significant within 1 ns.

We emphasize that the THz excitation is significantly different from optical excitation because hot electrons after electronic excitation by optical pulses excite a wide spectrum of phonon modes by electron-phonon coupling. The mechanism for the THz field excitation of the strain wave is due to direct coupling of the THz field to vibrational modes of BTO, exciting low-frequency optical phonons [11,18]. The absorbed energy dissipates into low-frequency acoustic phonons via phonon-phonon scattering on ps time scales. The THz source

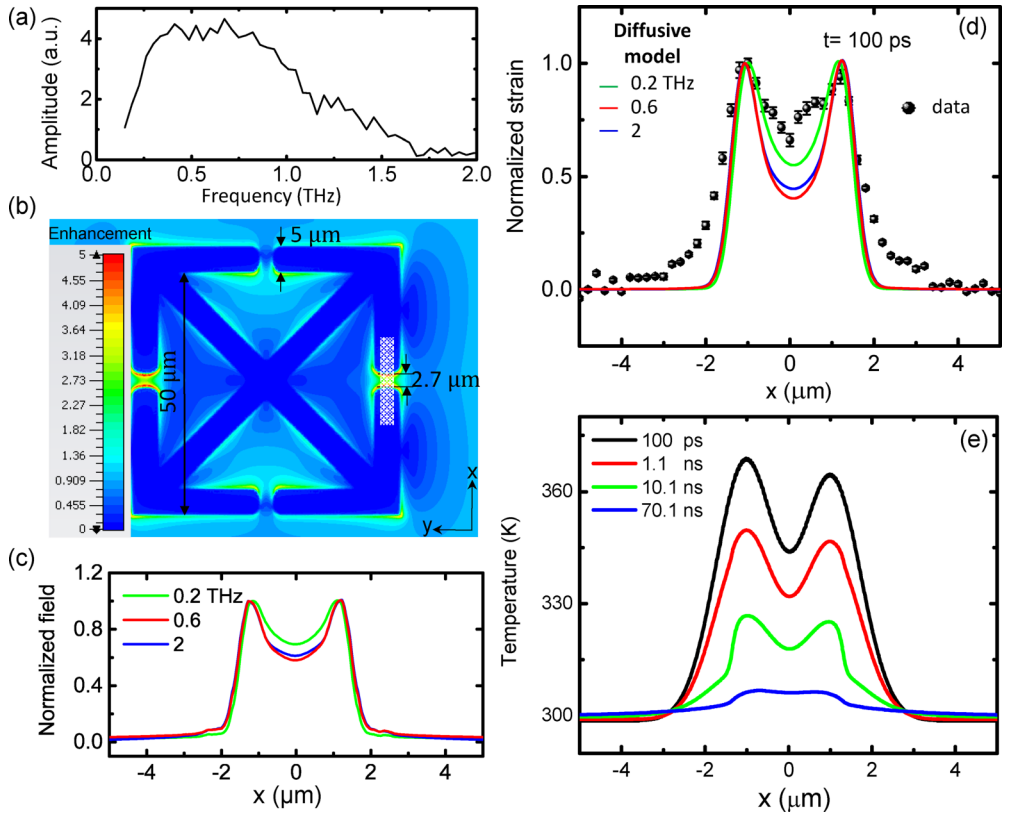

FIG. 4. (a) The spectrum of the incident THz field. (b) The calculated THz field distribution in the BTO layer around a split-ring resonator. The color bar shows the field enhancement factor. The white rectangular box across the gap shows the regime of 1D x-ray scanning probe along the x axis. (c) The line profiles of the THz field across the gap along the x axis in the BTO layer, simulated with different incident THz frequencies. The profile at 0.2 and 2 THz was scaled by a factor of 0.47 and 2.3 to compare with the profile at 0.6 THz. (d) Measured (dots) and simulated (solid curves) strain profile based on the diffusive model at 100 ps. (e) Fitted (black) and simulated (other colors) temperature profiles inside BTO thin film based on diffusive thermal transport model.

used here has a confined spectrum peaked around 0.6 THz with a cutoff frequency of 1.7 THz as shown in Fig. 4(a). Therefore, the ionic heating of BTO is due to selective excitation of low-frequency phonons up to 1.7 THz, neglecting phonon up-conversion processes. In a comparison of THz excitation, optical pulses excite electron-hole pairs which subsequently transfer energy to the lattice to excite the optical and acoustic phonon modes via electron-phonon coupling and deformation potential [32]. At 100-ps time scales, the lattice temperature rises and the excited phonon spectrum follows the blackbody spectrum, which is peaked around 30 THz near room temperature. The subsequent phonon-phonon interaction excites nonequilibrium acoustic phonon modes that can have ns lifetime [33,34]. Therefore, the optical pulses excite electronic degrees of freedom and result in a broad phonon spectrum, while the use of a THz field only selectively excites low-frequency phonons. Using near-field enhancement, this selective excitation is confined in a nanoscale volume as shown in Figs. 4(b) and 4(c), allowing the creation of a nonthermal phonon wave packet with narrow-band low-frequency phonon population.

To gain insight into phonon transport upon selective THz excitation, atomistic modeling of BTO [35–38] was performed to calculate the phonon band structure [35,39], the spectral group velocities, relaxation times [40–42], and mean free paths of all phonon [30]. Figure 5 shows that the MFPs of low-frequency phonons are significantly longer than the averaged

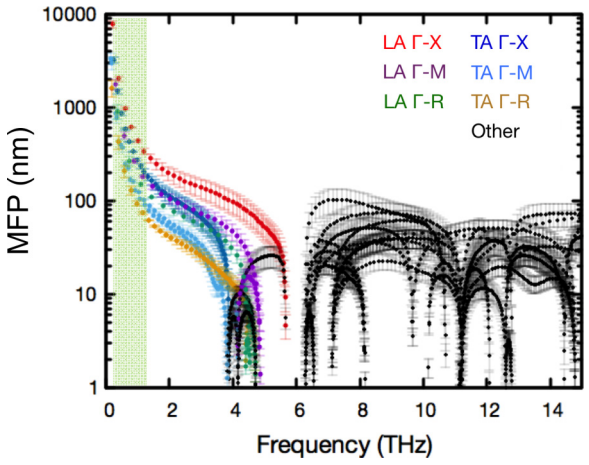

FIG. 5. The calculated phonon mean-free path as a function of frequency. The green overlay around 0.2 to 1.7 THz shows the spectral region that is covered by the pump THz pulse. Select phonon modes, longitudinal acoustic (LA) vs transverse acoustic (TA) along three Brillouin zone (BZ) branches, are color-coded as appropriate. Γ refers to the origin of the BZ, X is (0.5,0,0), M is (0.5,0.5,0), and R is (0.5,0.5,0.5).

MFP of all phonon modes, consistent with previous molecular dynamics simulations [27]. Since x-ray specular reflection is only sensitive to the out-of-plane lattice strain, the measured strain broadening is dominated by the transverse acoustic (TA) phonon modes. We calculated the spectral-weighted MFP of the TA modes, $\text{MFP} = \int_0^\infty f(\omega)\text{MFP}_{\text{TA}}(\omega)d\omega / \int_0^\infty f(\omega)d\omega$, across the THz excitation spectrum $f(\omega)$, marked by the light-green area in Fig. 5. The result is 528 ± 25 nm, which qualitatively agrees with the broadening of the measured strain profile of 465 ± 58 nm. This agreement further supports the claim that the observed strain-profile broadening is a result of ballistic phonon transport [27,43]. The combined experimental and theoretical investigation therefore demonstrates that energy transport processes can be effectively controlled at the nanoscales by engineering the excitation spectrum.

At later times, as shown in Fig. 3(b), we did not observe further broadening of the profile. This suggests that the phonon MFP has an upper bound of ∼500 nm. Beyond this length scale, the dominant energy transport is through diffusive transport. The lack of further broadening of the strain profile after 100 ps directly supports the hypothesis that the in-plane heat transport transitions from ballistic to diffusive on a length scale of ∼500 nm. The observation of diffusive transport at long time- and length scales is consistent with the recent measurement of strain evolution upon localized optical excitation in $BiFeO_3$ films [44], in which the excitation gradient on the length scale of 2 μm is longer than the MFP of optically excited phonons such that no broadening of the strain profile was observed. The lack of further broadening at later time also supports the direct excitation of phonon modes by the incident THz field rather than a thermal gradient. If the excited strain originated from a spatial gradient of the in-plane temperature profile, the excited acoustic phonon spectrum would be centered around a frequency $\frac{v}{d} \sim 0.03$ THz [45], where d is the excitation gradient approximated as half of $1/e^2$ width of the THz field distribution. These low-frequency acoustic phonons have much longer MFP on the order of several micrometers. The thermal excitation mechanism of the strain profile would thus yield a further broadening of strain profile at later times, which was not observed. In addition, the possibility that the excitation of the BTO film arose due to the heating of the gold surface by the THz field can be eliminated. This is because the temperature rise of the gold upon THz excitation is only a few degrees estimated using the deposition energy and heat capacity of gold, and the thermal transport from gold to BTO film takes place on much longer ns time scales.

In conclusion, we created and imaged a tailored phonon wave packet in materials using metamaterial-enhanced THz excitation. The selective excitation of acoustic phonons and the spatial confinement of this excitation is the key to producing a strain profile with a lateral extension less than the MFP of its contained phonon modes. We subsequently imaged the evolution of the strain profile in a ferroelectric BTO thin film by time-resolved hard x-ray diffraction microscopy. We found that, within 100 ps, the in-plane broadening of the strain profile was driven by a ballistic transport process on the hundreds of nm length scale, significantly longer than the average MFP of all phonons and can be directly compared with the predictions of molecular dynamics modeling. On ns time scales, the evolution of the strain profile followed diffusive thermal transport. These measurements have captured a fundamental nanoscale energy process that spans from ballistic to diffusive over nm to μm length scales and ps to ns time scales. The demonstrated technique opens up opportunities for manipulating nanoscale phenomena transiently using metamaterials and provides a tool for direct imaging of structural changes in real space. It also avoids the complication associated with the removal of samples under metamaterials in near-field THz-pump/x-ray probe experiments [19]. Future development, including enhancing the temporal resolution using x-ray free-electron lasers and spatial resolution using coherent x-ray diffraction imaging, will greatly extend the demonstrated spatiotemporally resolved capability to tackle problems in interdisciplinary research areas such as nanoscale energy transport, metamaterials and plasmonic enhancement, nanoscale imaging, and ultrafast materials science.

This work was supported by US Department of Energy (DOE), Basic Energy Sciences, Materials Sciences and Engineering Division. H.W., L.W.M., and J.F. acknowledge support from the Department of Energy under Grant No. DE-SC0012375. The use of Advanced Photon Source and Center for Nanoscale Materials is supported by the US DOE, Office of Science, Office of Basic Energy Sciences under Contract No. DE-AC02-06CH11357. This research used computational resources of the National Energy Research Scientific Computing Center, a DOE Office of Science User Facility supported by the Office of Science of the US DOE under Contract No. DE-AC02-05CH11231. A.M.L. and F.C. acknowledge support from the DOE, Basic Energy Sciences, Materials Science and Engineering under Contract No. DE-AC02-76SF00515. P.G.E. and J.P. were supported by the US DOE Office of Science Basic Energy Sciences through Contract No. DE-FG02-04ER46147. A.R.D. acknowledges support from the Army Research Office under Grant No. W911NF-14-1-0104.

[1] A. A. Balandin, IEEE Potentials **21**, 11 (2002).

[2] D. G. Cahill, P. V. Braun, G. Chen, D. R. Clarke, S. Fan, K. E. Goodson, P. Keblinski, W. P. King, G. D. Mahan, and A. Majumdar, Appl. Phys. Rev. **1**, 011305 (2014).

[3] A. M. Marconnet, M. A. Panzer, and K. E. Goodson, Rev. Mod. Phys. **85**, 1295 (2013).

[4] J. A. Johnson, A. A. Maznev, J. Cuffe, J. K. Eliason, A. J. Minnich, T. Kehoe, C. M. S. Torres, G. Chen, and K. A. Nelson, Phys. Rev. Lett. **110**, 025901 (2013).

[5] Y. Hu, L. Zeng, A. J. Minnich, M. S. Dresselhaus, and G. Chen, Nat. Nanotechnol. **10**, 701 (2015).

[6] L. Zeng, K. C. Collins, Y. Hu, M. N. Luckyanova, A. A. Maznev, S. Huberman, V. Chiloyan, J. Zhou, X. Huang, K. A. Nelson, and G. Chen, Sci. Rep. **5**, 17131 (2015).

[7] M. E. Siemens, Q. Li, R. Yang, K. A. Nelson, E. H. Anderson, M. M. Murnane, and H. C. Kapteyn, Nat. Mater. **9**, 26 (2009).

[8] T. Kubacka, J. A. Johnson, M. C. Hoffmann, C. Vicario, S. de Jong, P. Beaud, S. Grubel, S.-W. Huang, L. Huber, L. Patthey,

Y.-D. Chuang, J. J. Turner, G. L. Dakovski, W.-S. Lee, M. P. Minitti, W. Schlotter, R. G. Moore, C. P. Hauri, S. M. Koohpayeh, V. Scagnoli, G. Ingold, S. L. Johnson, and U. Staub, Science **343**, 1333 (2014).

[9] T. Kampfrath, A. Sell, G. Klatt, A. Pashkin, S. Mährlein, T. Dekorsy, M. Wolf, M. Fiebig, A. Leitenstorfer, and R. Huber, Nat. Photonics **5**, 31 (2010).

[10] I. Katayama, H. Aoki, J. Takeda, H. Shimosato, M. Ashida, R. Kinjo, I. Kawayama, M. Tonouchi, M. Nagai, and K. Tanaka, Phys. Rev. Lett. **108**, 097401 (2012).

[11] M. Kozina, T. van Driel, M. Chollet, T. Sato, J. M. Glownia, S. Wandel, M. Radovic, U. Staub, and M. C. Hoffmann, Struct. Dyn. **4**, 054301 (2017).

[12] H.-T. Chen, A. J. Taylor, and N. Yu, Rep. Prog. Phys. **79**, 076401 (2016).

[13] M. A. Seo, H. R. Park, S. M. Koo, D. J. Park, J. H. Kang, O. K. Suwal, S. S. Choi, P. C. M. Planken, G. S. Park, N. K. Park, Q. H. Park, and D. S. Kim, Nat. Photonics **3**, 152 (2009).

[14] S. Bagiante, F. Enderli, J. Fabiańska, H. Sigg, and T. Feurer, Sci. Rep. **5**, 8051 (2015).

[15] S. Xiong, K. Sääskilahti, Y. A. Kosevich, H. Han, D. Donadio, and S. Volz, Phys. Rev. Lett. **117**, 025503 (2016).

[16] M. Liu, H. Y. Hwang, H. Tao, A. C. Strikwerda, K. Fan, G. R. Keiser, A. J. Sternbach, K. G. West, S. Kittiwatanakul, J. Lu, S. A. Wolf, F. G. Omenetto, X. Zhang, K. A. Nelson, and R. D. Averitt, Nature (London) **487**, 345 (2012).

[17] A. X. Gray, M. C. Hoffmann, J. Jeong, N. P. Aetukuri, D. Zhu, H. Y. Hwang, N. C. Brandt, H. Wen, A. J. Sternbach, S. Bonetti *et al.*, arXiv:1601.07490.

[18] F. Chen, Y. Zhu, S. Liu, Y. Qi, H. Y. Hwang, N. C. Brandt, J. Lu, F. Quirin, H. Enquist, P. Zalden, T. Hu, J. Goodfellow, M.-J. Sher, M. C. Hoffmann, D. Zhu, H. Lemke, J. Glownia, M. Chollet, A. R. Damodaran, J. Park, Z. Cai, I. W. Jung, M. J. Highland, D. A. Walko, J. W. Freeland, P. G. Evans, A. Vailionis, J. Larsson, K. A. Nelson, A. M. Rappe, K. Sokolowski-Tinten, L. W. Martin, H. Wen, and A. M. Lindenberg, Phys. Rev. B **94**, 180104(R) (2016).

[19] M. Kozina, M. Pancaldi, C. Bernhard, T. van Driel, J. M. Glownia, P. Marsik, M. Radovic, C. A. F. Vaz, D. Zhu, S. Bonetti, U. Staub, and M. C. Hoffmann, Appl. Phys. Lett. **110**, 081106 (2017).

[20] C. Lange, T. Maag, M. Hohenleutner, S. Baierl, O. Schubert, E. R. J. Edwards, D. Bougeard, G. Woltersdorf, and R. Huber, Phys. Rev. Lett. **113**, 227401 (2014).

[21] G. Scalari, C. Maissen, D. Turčinková, D. Hagenmüller, S. De Liberato, C. Ciuti, C. Reichl, D. Schuh, W. Wegscheider, M. Beck *et al.*, Science **335**, 1323 (2012).

[22] Y. Zhu, Z. Cai, P. Chen, Q. Zhang, M. J. Highland, I. W. Jung, D. A. Walko, E. M. Dufresne, J. Jeong, M. G. Samant, S. S. P. Parkin, J. W. Freeland, P. G. Evans, and H. Wen, Sci. Rep. **6**, 21999 (2016).

[23] A. J. L. Adam, J. Infrared, Millimeter, Terahertz Waves **32**, 976 (2011).

[24] F. Blanchard, A. Doi, T. Tanaka, and K. Tanaka, Annu. Rev. Mater. Res. **43**, 237 (2013).

[25] M. Highland, B. C. Gundrum, Y. K. Koh, R. S. Averback, D. G. Cahill, V. C. Elarde, J. J. Coleman, D. A. Walko, and E. C. Landahl, Phys. Rev. B **76**, 075337 (2007).

[26] M. E. Pumarol, M. C. Rosamond, P. Tovee, M. C. Petty, D. A. Zeze, V. Falko, and O. V. Kolosov, Nano Lett. **12**, 2906 (2012).

[27] B. F. Donovan, B. M. Foley, J. F. Ihlefeld, J.-P. Maria, and P. E. Hopkins, Appl. Phys. Lett. **105**, 082907 (2014).

[28] J. Hebling, K.-L. Yeh, M. C. Hoffmann, B. Bartal, and K. A. Nelson, J. Opt. Soc. Am. B **25**, B6 (2008).

[29] Q. Wu and X.-C. Zhang, Appl. Phys. Lett. **71**, 1285 (1997).

[30] See Supplemental Material at http://link.aps.org/supplemental/10.1103/PhysRevMaterials.1.060601 for details of the experiments, data analysis, and simulations.

[31] J.-M. Manceau, P. A. Loukakos, and S. Tzortzakis, Appl. Phys. Lett. **97**, 251904 (2010).

[32] D. M. Fritz, D. A. Reis, B. Adams, R. A. Akre, J. Arthur, C. Blome, P. H. Bucksbaum, A. L. Cavalieri, S. Engemann, S. Fahy, R. W. Falcone, P. H. Fuoss, K. J. Gaffney, M. J. George, J. Hajdu, M. P. Hertlein, P. B. Hillyard, M. Horn-von Hoegen, M. Kammler, J. Kaspar, R. Kienberger, P. Krejcik, S. H. Lee, A. M. Lindenberg, B. McFarland, D. Meyer, T. Montagne, E. D. Murray, A. J. Nelson, M. Nicoul, R. Pahl, J. Rudati, H. Schlarb, D. P. Siddons, K. Sokolowski-Tinten, Th. Tschentscher, D. von der Linde, and J. B. Hastings, Science **315**, 633 (2007).

[33] R. Shayduk, M. Herzog, A. Bojahr, D. Schick, P. Gaal, W. Leitenberger, H. Navirian, M. Sander, J. Goldshteyn, I. Vrejoiu, and M. Bargheer, Phys. Rev. B **87**, 184301 (2013).

[34] M. Trigo, J. Chen, V. H. Vishwanath, Y. M. Sheu, T. Graber, R. Henning, and D. A. Reis, Phys. Rev. B **82**, 235205 (2010).

[35] S. Tinte, M. G. Stachiotti, M. Sepliarsky, R. L. Migoni, and C. O. Rodriguez, J. Phys.: Condens. Matter **11**, 9679 (1999).

[36] R. W. Hockney and J. W. Eastwood, *Computer Simulation Using Particles* (Taylor & Francis, New York, 1988).

[37] M. B. Smith, K. Page, T. Siegrist, P. L. Redmond, E. C. Walter, R. Seshadri, L. E. Brus, and M. L. Steigerwald, J. Am. Chem. Soc. **130**, 6955 (2008).

[38] D. G. Doran, J. Appl. Phys. **39**, 40 (1968).

[39] A. Togo and I. Tanaka, Scr. Mater. **108**, 1 (2015).

[40] J. A. Thomas, J. E. Turney, R. M. Iutzi, C. H. Amon, and A. J. H. McGaughey, Phys. Rev. B **81**, 081411(R) (2010).

[41] T. Feng, B. Qiu, and X. Ruan, J. Appl. Phys. **117**, 195102 (2015).

[42] J. Callaway, Phys. Rev. **113**, 1046 (1959).

[43] A. A. Maznev, F. Hofmann, A. Jandl, K. Esfarjani, M. T. Bulsara, E. A. Fitzgerald, G. Chen, and K. A. Nelson, Appl. Phys. Lett. **102**, 041901 (2013).

[44] J. Park, Q. Zhang, P. Chen, M. P. Cosgriff, J. A. Tilka, C. Adamo, D. G. Schlom, H. Wen, Y. Zhu, and P. G. Evans, Rev. Sci. Instrum. **86**, 083904 (2015).

[45] C. Thomsen, H. T. Grahn, H. J. Maris, and J. Tauc, Phys. Rev. B **34**, 4129 (1986).